Computation of Ionization in Re-Entry Flowfields

JOHN S. EVANS,* CHARLES J. SCHEXNAYDER,* AND PAUL W. HUBER†
NASA Langley Research Center, Hampton, Va.

Techniques are described for the computation of electron concentration profiles in the shock layer surrounding a blunt-nosed vehicle during entry into the atmosphere at near-orbital entry speed and at altitudes where ion diffusion effects can be neglected. Emphasis is laid on a careful treatment of finite rate chemistry and of the effects of boundary layer. A streamtube approach is used to calculate gas composition in both the inviscid and viscous parts of the shock layer. The effects of finite rate chemistry on streamline position and shock shape are included. Also accounted for are the effects of boundary-layer displacement, streamline swallowing, and vorticity interaction normal to flow direction. The major influence on the magnitude and shape of electron concentration profiles during re-entry is found to be finite rate chemistry, although the boundary layer has an important influence on profile shape at high altitude. Incomplete reaction systems are shown to be capable of causing large errors in the profiles.

Nomenclature

$\hat{C}_p$ = normalized pressure coefficient, $(p - p_1)/(p_2 - p_1)$
c_p = specific heat at constant pressure of the mixture
d_N = body nose diameter
H_i = enthalpy of the ith species
M = Mach number
N_A = Avogadro constant
N_e = electron concentration
p = gas pressure
Q_{ij} = contribution of the jth reaction rate to the rate of change of the ith species
R = universal gas constant
r_s = distance from body axis to shock front
r_b = distance from body axis to body surface
S = gas entropy
s = distance along streamline from shock front
T = gas temperature
T_r = 273.16°K
u = gas flow speed
x = distance along body axis from nose surface
y = distance along perpendicular to body surface, measured from body surface
γ_e = specific concentration of electrons
γ_i = specific concentration of the ith species
Δ = value of y at the shock front for a given value of x/d_N
δ = boundary-layer thickness as computed from classical boundary-layer theory
δ^* = boundary-layer displacement thickness
δ_m = effective boundary-layer thickness for the merged profile
ϵ = angle between axis and tangent to shock wave
η = $\Sigma\gamma_i$
θ_b = angle between axis and tangent to spherical nose
θ_c = angle between axis and conical body surface
ρ = gas density

Subscripts and superscripts

b = body
c = cone
s = value at shock front
1 = freestream value
2 = value at shock front for stagnation streamline
$'$ = transformed value of y (see Appendix B)

I. Introduction

IN order to quantitatively assess the radio attenuation which occurs during spacecraft atmospheric entry it is necessary to calculate accurately ionization profiles in the flowfield aft of the nose-flow region, since this is where antennas are usually placed. In the case of slender sharp-nosed bodies most of the ionization occurs within the highly dissipative boundary-layer flow region which is generally thin relative to the shock layer. Because these ionization profiles are close to the body surface and contain strong ion gradients, the effects of diffusion, surface recombination, ablation, etc., are important considerations in computing the ionization.[1,2] However, for blunt-nosed bodies the shock layer ionization is mainly produced in the strong shock inviscid nose-flow region and persists during expansion of the flow around the shoulder and into the afterbody region. This ionized layer may occupy a substantial fraction of the shock layer for the first few nose diameters of flow length, and the boundary layer is often nondissipative in this region. Therefore, at low altitudes where the boundary layer is thin, it plays no significant role in the ionization except for the case of large ablation blowing, where the ablated material is contaminated with easily ionizable impurities. At intermediate altitudes, where the boundary-layer thickness becomes comparable with the high entropy ionized layer, the effects of displacement and vorticity interaction have an important influence on the profile shape but not much effect on the peak level of ionization. For these two altitude regimes air chemical kinetics is the dominant influence on ionization level, provided that the concentration of easily ionized ablation impurities is sufficiently small. For still higher altitudes (but before the boundary layer fills the shock layer) the effects of ambipolar electron-ion diffusion and of surface recombination produce large changes in both profile shape and ionization level.[3,4]

In this paper techniques for computing ionization profiles for blunt-nosed re-entry bodies are presented. Emphasis is on careful consideration of the chemical kinetics and of the effects of boundary-layer vorticity interaction. The computations are limited to orbital entry velocity and below, to the case of no ionizable ablation impurities, and to the altitude range below that at which diffusion effects are important. The body considered herein is a 9° half-angle cone blunted with a 30.5 cm diam spherical nose, and at zero angle of incidence to the entry flight path. The major effects of radio attenuation occur within these limitations on entry conditions with the exception of attenuation of the lower frequency signals (VHF) which starts at an altitude above the diffusion limiting altitude (230,000 ft for d_N = 30.5 cm).

The technique, which includes several machine programs and one hand operation, is tailored for the computation of detailed ionization profiles throughout the supersonic portion

Received June 5, 1969; revision received November 17, 1969.
* Aerospace Engineer, Planetary Gas Kinetics Section.
† Head, Planetary Gas Kinetics Section, Aero-Physics Division.

of the shock layer at many points along the entry trajectory. Basically, the uncoupled streamtube approach is used, but coupling is achieved, in effect, by iteration of the streamtube and shock layer programs. A complete reaction system is employed along the streamlines both in the inviscid flow region and in the merged boundary-layer inviscid flow region, but in the latter region the streamline locations and boundary conditions are changed according to the dictates of the boundary-layer solutions and the hand merging procedure. Although the method used is not fundamentally different from previous methods for blunt bodies with regard to use of the streamtube technique,[5] boundary-layer swallowing,[3] and boundary-layer merging,[6] some of the innovations employed lead to more precise specification of the ionization profiles. The unique features include the use of finite rate nonequilibrium shock layer solutions for determination of shock shape, for location of inviscid streamlines, and for specification of edge conditions for boundary-layer swallowing and merging. Also included are illustrations of the sensitivity of the profiles to the chemical kinetic rates and to the use of incomplete reaction systems.

II. Procedures and Typical Calculated Results

A. Definition of Inviscid Flowfield

Figure 1 shows the sphere-cone body and a typical streamline path in the surrounding flowfield. A number of methods for finding the details of such a flowfield have been published in the literature. In the subsonic region either the direct[7] or the inverse[8] approach is used, and the solution is continued in the supersonic region by the method of characteristics. In these methods the gas properties are usually assumed to be either in complete thermochemical equilibrium or to have a frozen composition. The computer time and professional skill required to obtain a complete flowfield solution at one flight speed and altitude is substantial. When finite rate reactions are included[9] the required effort goes up tremendously.

The streamtube approach to finite rate flow property determination avoids the complexity of the coupled approach by utilizing the streamline paths and boundary conditions along the streamlines as obtained from equilibrium or frozen flowfield solutions. The error involved in the resulting ionization profiles is usually small, except in the nose regions. In the streamtube approach used herein streamline positions are adjusted for the effects of finite rate chemistry through a shock layer mass conservation program to be discussed later.

Furthermore, the necessity to initially calculate an equilibrium or frozen flowfield for each of the many trajectory points needed for the re-entry can also be avoided, with small error, by utilizing normalized plots of existing solutions. The normalizations which were used to construct inviscid streamline positions and pressure distributions are shown in Figs. 2 and 3. They were derived from a number of equilibrium and frozen flowfield solutions.[8,10] In the forms shown these parameters are relatively independent of M_1, θ_c, d_N, and gas properties in the hypersonic regime $15 > M_1 > 30$, in the

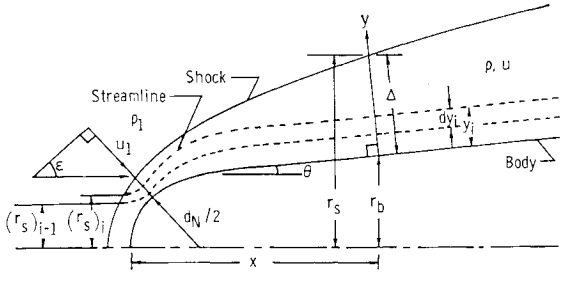

Fig. 1 Flowfield and typical streamline paths.

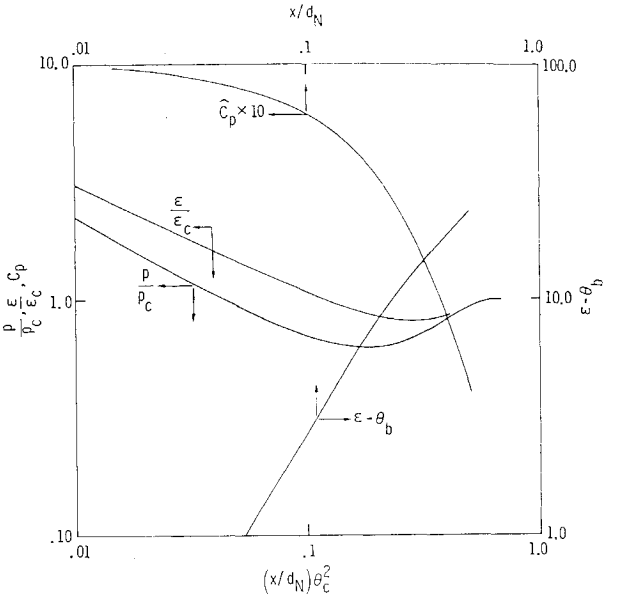

Fig. 2 Normalized shock shape and body pressure for equilibrium inviscid flow over a spherically blunted 9° half-angle cone.

range of cone angles $6 < \theta_c < 15$, and for the altitude range $70 \times 10^3 <$ alt $< 230 \times 10^3$ ft.‡ Even though computations were made only for a 9° half-angle blunt-cone-shaped body, θ_c is larger than 9° at the higher altitudes where actual cone angles are replaced by larger effective cone angles in order to account for the displacement thickness of the boundary layer.

For a given set of flight conditions pressure distributions were constructed as follows: 1) the shock shape ($\epsilon - \theta_b$ vs x/d_N and ϵ/ϵ_c vs $\theta_c^2 x/d_N$) and the body pressure distribution ($\hat{C}_p$ vs x/d_N and p/p_c vs $\theta_c^2 x/d_N$) are found, where ϵ_c and p_c are sharp cone values based on M_1, θ_c, and an assumed specific heat ratio; 2) at given x/d_N the variation of pressure and entropy across the shock layer is found from Fig. 3. The entropy parameter is used only for determining streamline

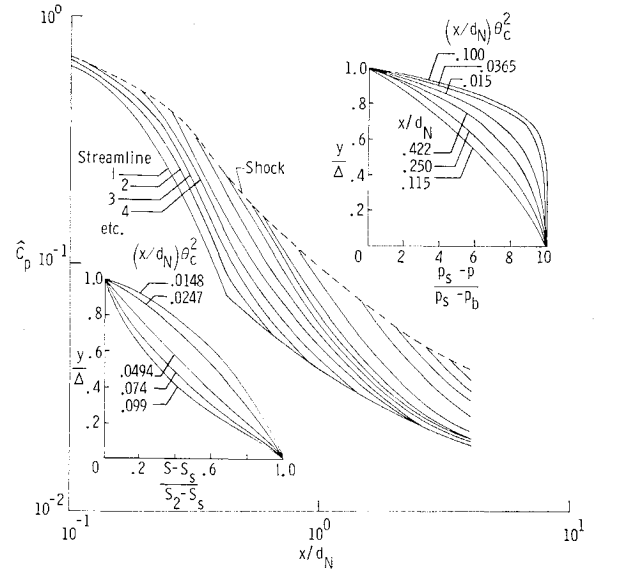

Fig. 3 Normalized pressure profiles, normalized entropy profiles, and streamline pressure distribution for equilibrium inviscid flow over a spherically blunted 9° half-angle cone.

‡ The upper altitude limit varies with body scale. The limit shown is appropriate for $d_N = 30.5$ cm.

Table 1 Constants for use in reaction rate formulas

i	Reaction	μ_i	D_i	σ_i (cm^2)	i	Reaction	μ_i	D_i	σ_i (cm^2)
1	$O_2 + O_2 \rightleftharpoons O + O + O_2$	16.000	217.34	14.60×10^{-16}	28	$O + NO \rightleftharpoons NO^+ + O^-$	10.435	330.70	1.00×10^{-16}
2	$O_2 + O \rightleftharpoons O + O + N_2$	14.934	217.34	7.75	29	$N + (O \text{ or } N) \rightleftharpoons N^+ + e^- + (O \text{ or } N)$	7.000	617.80	1.00
3	$O_2 + O \rightleftharpoons O + O + O$	10.667	217.34	60.00	30	$O + (O \text{ or } N) \rightleftharpoons O^+ + e^- + (O \text{ or } N)$	8.000	578.40	1.00
4	$O_2 + N \rightleftharpoons O + O + N$	9.739	217.34	6.72	31	$N_2 + NO^+ \rightleftharpoons N_2^+ + NO$	14.50	268.90	20.00
5	$O_2 + NO \rightleftharpoons O + O + NO$	15.484	217.34	5.00	32	$N + NO^+ \rightleftharpoons N^+ + NO$	9.55	224.80	20.00
6	$N_2 + O_2 \rightleftharpoons N + N + O_2$	14.934	414.50	10.30	33	$O + NO^+ \rightleftharpoons O^+ + NO$	10.40	185.2	20.00
7	$N_2 + N_2 \rightleftharpoons N + N + N_2$	14.000	414.50	16.50	34	$O_2 + NO^+ \rightleftharpoons O_2^+ + NO$	15.50	120.20	20.00
8	$N_2 + O \rightleftharpoons N + N + O$	10.182	414.50	6.45	35	$N_2 + O_2 \rightleftharpoons N_2^+ + O_2$	14.90	148.70	20.00
9	$N_2 + N \rightleftharpoons N + N + N$	9.334	414.50	72.00	36	$N + O_2^+ \rightleftharpoons N^+ + O_2$	9.74	104.50	20.00
10	$N_2 + NO \rightleftharpoons N + N + NO$	14.483	414.50	7.00	37	$O + O_2^+ \rightleftharpoons O^+ + O_2$	10.70	65.00	20.00
11	$NO + O_2 \rightleftharpoons N + O + O_2$	15.484	275.74	2.94	38	$N_2 + O^+ \rightleftharpoons N_2^+ + O$	10.20	83.70	20.00
12	$NO + N_2 \rightleftharpoons N + O + N_2$	14.483	275.74	3.12	39	$N + O^+ \rightleftharpoons N^+ + O$	7.47	39.51	20.00
13	$NO + O \rightleftharpoons N + O + O$	10.435	275.74	6.06	40	$N_2 + N^+ \rightleftharpoons N_2^+ + N$	9.34	44.19	20.00
14	$NO + N \rightleftharpoons N + O + N$	9.545	275.74	11.30	41	$O^- + M \rightleftharpoons O + e^- + M$	10.00	82.48	10.00
15	$NO + NO \rightleftharpoons N + O + NO$	15.000	275.74	14.80	42	$O_2^- + M \rightleftharpoons O_2 + e^- + M$	15.00	19.55	10.00
16	$O + N_2 \rightleftharpoons NO + N$	10.182	138.93	2.69	43	$O_2 + e^- \rightleftharpoons O^- + O$	5.4858×10^{-4}	155.14	0.10
17	$O + NO \rightleftharpoons O_2 + N$	10.435	71.24	1.10	44	$O + NO^+ \rightleftharpoons N^+ + O_2$	10.44	282.90	20.00
18	$O + O \rightleftharpoons O_2^+ + e^-$	8.000	294.85	0.025	45	$NO + NO^+ \rightleftharpoons N_2^+ + O_2$	15.00	188.60	20.00
19	$N + N \rightleftharpoons N_2^+ + e^-$	7.000	247.27	0.066	46	$O + NO^+ \rightleftharpoons O_2^+ + N$	10.40	178.40	20.00
20	$N + O \rightleftharpoons NO^+ + e^-$	7.467	117.69	0.076	47	$N + NO^+ \rightleftharpoons N_2^+ + O$	9.55	130.00	20.00
21	$N_2 + e^- \rightleftharpoons N_2^+ + e^- + e^-$	5.4858×10^{-4}	661.90	1.00	48	$N + NO^+ \rightleftharpoons O^+ + N_2$	9.55	46.31	20.00
22	$N + e^- \rightleftharpoons N^+ + e^- + e^-$	5.4858×10^{-4}	617.80	1.00	49	$NO + NO^+ \rightleftharpoons O_2^+ + N_2$	15.00	39.93	20.00
23	$O + e^- \rightleftharpoons O^+ + e^- + e^-$	5.4858×10^{-4}	578.40	1.00	50	$N_2 + O^+ \rightleftharpoons N^+ + NO$	10.18	178.40	20.00
24	$O_2 + e^- \rightleftharpoons O_2^+ + e^- + e^-$	5.4858×10^{-4}	513.00	1.00	51	$NO + O^+ \rightleftharpoons N^+ + O_2$	10.44	97.71	20.00
25	$NO + e^- \rightleftharpoons NO^+ + e^- + e^-$	5.4858×10^{-4}	393.00	1.00	52	$N + O_2^+ \rightleftharpoons O + NO$	9.74	6.80	20.00
26	$O + O \rightleftharpoons O^+ + O^-$	8.000	516.00	1.00	53	$O + N_2^+ \rightleftharpoons N^+ + NO$	10.18	94.74	20.00
27	$O + N \rightleftharpoons N^+ + O^-$	7.467	555.50	1.00	54	$O_2 + O^- \rightleftharpoons O_2^- + O$	10.67	42.93	20.00

locations in the shock layer by means of an entropy identification, which is chosen to be the entropy behind the equilibrium shock at its entry point into the shock layer§; 3) the resulting pressure distribution is curve fitted to provide pressure variation along streamlines (Fig. 3).

A standard network of flowfield points, composed of intersections between 20 numbered streamlines and 20 body station perpendiculars, was devised to provide convenient cross reference points between computer programs and as an aid in plotting results. At the beginning of work for given flight conditions an initial shock line is plotted. (This line is subject to later modification by mass-flow considerations.) Each of the numbered streamlines originates at the intersection of a body station line with the shock line. Initial conditions on a streamline are obtained by iterating the Rankine-Hugoniot shock equations for a gas of freestream composition and fully excited internal energy across an oblique shock tangent to the shock envelope at the entry point.

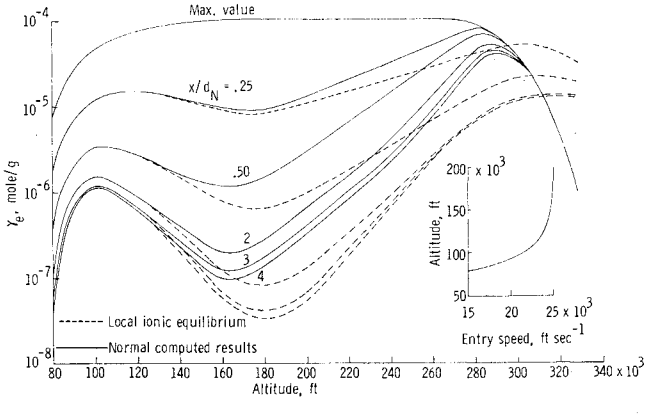

Fig. 4 Ionization level as a function of altitude for inviscid body streamline.

§ This entropy value is not used for any other purpose because of the nonequilibrium nature of the flow.

B. Integration along Streamtubes

The next step is to solve the quasi-one-dimensional fluid-flow equations and the finite rate chemical equations by means of step-by-step integration. These equations are written as follows:

$$\frac{\eta RT}{u_s^2}\left(\frac{1}{\rho_s}\frac{d\rho}{ds}\right) + \frac{\eta\rho RT_s}{\rho_s u_s^2}\left(\frac{1}{T_s}\frac{dT}{ds}\right) + \sum_{j=1}^{13}\frac{\eta_s\rho RT}{\rho_s u_s^2}\left(\frac{1}{\eta_s}\frac{d\gamma_j}{ds}\right) = \frac{1}{\rho_s u_s^2}\frac{dp}{ds} \quad (1)$$

$$\frac{\eta\rho RT_s(c_p/R)}{\rho_s u_s^2}\left(\frac{1}{T_s}\frac{dT}{ds}\right) + \sum_{j=1}^{13}\frac{\eta_s\rho RT(H_j/RT)}{\rho_s u_s^2}\left(\frac{1}{\eta_s}\frac{d\gamma_j}{ds}\right) = \frac{1}{\rho_s u_s^2}\frac{dp}{ds} \quad (2)$$

$$\sum_{j=1}^{13}\delta_{ij}\left(\frac{1}{\eta_s}\frac{d\gamma_i}{ds}\right) = \sum_{k=1}^{54} Q_{ik} \quad (3)$$

where δ_{ij} is the Kronecker delta. This way of formulating the problem is essentially that described in Ref. 11, in which the solution of the equations is also discussed.

The reaction system used is given in Table 1. The initial component species are assumed to be O_2(21%) and N_2 (79%). The list of species is O_2, N_2, O, N, NO, NO^+, O_2^+, N_2^+, O^+, N^+, e^-, O_2^-, and O^-. The specific rate constants for the molecular dissociation reactions (1–15) have the form[12]

$$k_{fi} = N_A\left(\frac{8RT}{\pi\mu_i}\right)^{1/2}\frac{4}{3\pi^{1/2}}\left(\frac{D_iT_r}{T}+\frac{1}{2}\right)^{3/2}\times \sigma_i\exp\left[-\left(\frac{D_iT_r}{T}+1\right)\right] \quad (4)$$

The specific rate constants for the remaining reactions have

the form

$$k_{fi} = N_A \left(\frac{8RT}{\pi\mu_i}\right)^{1/2} \sigma_i \exp\left[-\left(\frac{D_i T_r}{T}\right)\right] \quad (5)$$

The constants used in the equations are given in Table 1. All rates are written as forward rates in the endothermic direction. Reverse rates were obtained from the ratio $k_{fi}/k_{ri} = K_i$.

C. Profiles of Gas Properties in the Inviscid Flow

Profiles of all the gas properties (ρ, u, T, and p, as well as the concentrations of the species) are found by plotting the values computed at standard network points against y. Initially, y values are found from the normalized plots of Fig. 3, but these are improved by means of a computation (see Appendix A) which adjusts the y's so as to ensure conservation of mass flow at the nonequilibrium conditions.

D. Effect of Boundary Layer on the Electron Concentration Profiles

Although computer programs[1] for calculating boundary-layer flow properties along hypersonic bodies with coupled finite rate chemistry have been developed, these programs are all based on the classical boundary-layer problem, for which boundary-layer edge properties change slowly in the flow direction and for which inviscid flow gradients normal to the boundary-layer edge vanish. Such idealized conditions conflict with actual conditions in a thick boundary layer where vorticity due to the curved bow shock is large. Another deterrent to the use of coupled boundary-layer programs for ionized flowfield calculations arises from the mathematical complications introduced by including a large number of finite rate reactions.

In order to fulfill the need to compute with a reasonably complete reaction system and to be able at the same time to include effects of vorticity interaction, streamtubes from the inviscid region are continued into the boundary layer and the number of matching parameters along the streamtubes are increased from one to three. (This is done because of the necessity to delete the momentum and energy conservation equations.) Thus, the problem reduces to determination of streamline positions in the boundary layer and of the variation of the additional matching parameters. A three-step procedure is used to find these properties, as described in Appendix B.

III. Discussion of Results

A. Electron Concentration on an Inviscid Streamline

Figure 4 is a plot against altitude of γ_e at various body stations. The one exception is the "max value" curve, which shows the maximum value reached by γ_e on the streamline. The quantity γ_e is related to electron concentration by the equation $N_e = N_A \rho \gamma_e$ and is chosen because it displays the electron content independent of gas density. The curves are invalid for practical application above an altitude at which ambipolar diffusion begins to become dominant. This altitude is about 230,000 ft for $d_N = 30.5$ cm.

The curves of Fig. 4 must be analyzed in terms of their relation to the velocity-altitude plot of the corresponding entry trajectory. (Shown as a sketch on the figure.) From the highest altitudes down to about 150,000 ft the vehicle is moving with nearly constant speed and at rapidly decreasing altitude. Correlated with this is the flatness of the max value curve until speed begins to decrease, which indicates that the degree of ionization reached behind the shock front is strongly dependent on the nearly constant vehicle speed and is nearly independent of altitude. The max value curve falls off at high altitude because the reactions are too slow to produce the required electrons before production is diminished in the expansion over the shoulder of the vehicle.

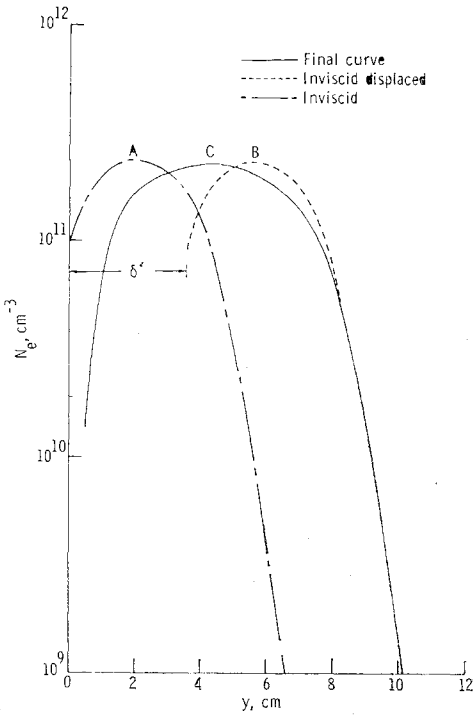

Fig. 5 Steps in the calculation of an electron concentration profile; altitude = 233,000 ft, $x/d_N = 4$.

Below 150,000 ft the reactions are fast enough for rapid production of electrons but decreased vehicle speed produces lower temperatures (lower ionization) behind the shock.

The amount of electron recombination occurring during expansion of the streamline at various altitudes is indicated by the spacing of body station curves below the max value curve. That no recombination occurs at the highest altitudes is evident from the merging of these curves into the max value curve there. The dotted lines in Fig. 4 are local ionic equilibrium curves. They were calculated by assuming that all the reactions for charged particles are infinitely fast, so that equilibrium of the charged species at local temperature and density is achieved. These curves are useful for comparison with the finite rate results.

It is noted that electron recombination to the local ionic equilibrium level is incomplete at most altitudes not only because reaction times are comparable to flow time but also because cooling by expansion continues to depress the local ionic equilibrium curves as the flow proceeds from one body station to another. However, it is complete at the lower altitudes, where heat released by recombining atoms maintains gas temperature at a relatively high level. The local ionic equilibrium curves constitute a lower limit for the recombination of electrons.

B. Electron Concentration Profiles

The effects of applying the procedures described herein are illustrated in Fig. 5. Curve A is a plot of inviscid streamtube results against y coordinates obtained from the mass conservation program (Appendix A). Displacement of curve A by the boundary-layer-displacement thickness led to curve B. The final result, curve C, includes re-evaluation of gas composition inside the boundary layer as well as recalculation of y coordinates in the boundary layer based on merged boundary layer and inviscid profiles (Appendix B).

C. Demonstration of the Importance of Using an Adequate System of Charge Transfer Reactions

The kinetics of charge transfer is very important under some circumstances. For example, atomic ions would persist

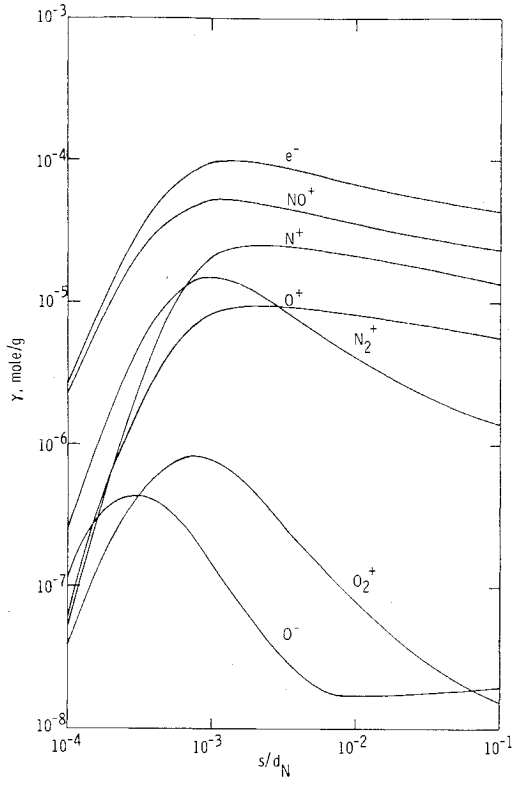

Fig. 6 Initial rise of charged species on a streamline; body streamline, altitude = 156,000 ft.

for long times at high altitudes if they were unable to transfer their charge to molecules, which recombine by the fast dissociative recombination reactions. Charge transfer also allows molecular charge to be concentrated on molecules having the lowest ionization potential (NO^+ in air). Thus the "self-limiting" level[13] of N_e depends on only one reaction and is lower than it would otherwise be. Figures 6 and 7(a) show the variations of ion concentrations along an inviscid streamline as calculated for an entry speed of 25,000 fps and altitude 156,000 ft with the reactions found in Table 1. (This set of reactions is hereafter referred to as the normal set.)

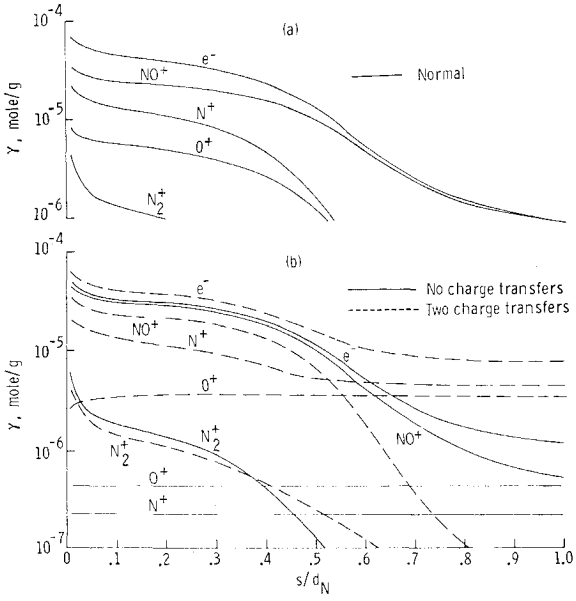

Fig. 7 Body streamline variation of charged particles; altitude = 156,000 ft.

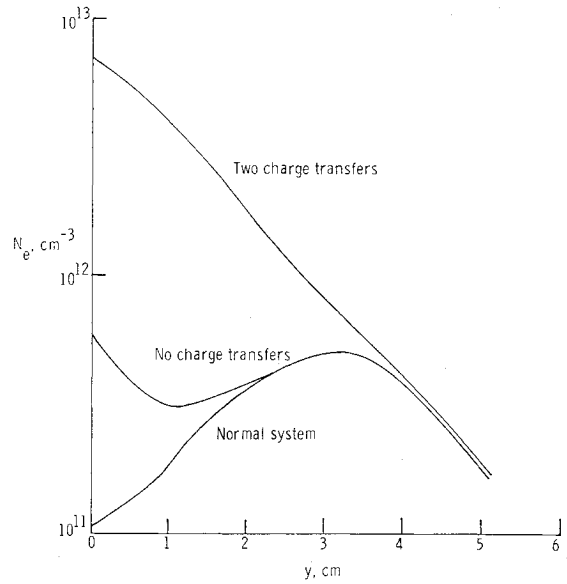

Fig. 8 Illustration of the influence of charge transfer reactions on Ne profiles; altitude = 156,000 ft, $x/d_N = 4$.

The effect of leaving out all charge transfer reactions is shown in Fig. 7b for which only reactions 1–25, plus reactions 29 and 30, were used. The main difference between Figs. 7a and 7b is in the behavior of O^+ and N^+. The initial values on Fig. 7b are lower, and there is no decrease at all along the streamline. The initial values are lower because there is no charge transfer to augment the production of O^+ and N^+ by reactions 22, 23, 29, and 30. The failure of O^+ and N^+ to disappear by reversal of the reactions which produced them is attributed to the ineffectiveness of three-body reactions at low density.

The effect of including only a limited amount of charge transfer[6] is also illustrated in Fig. 7b, for which the reactions $O + O_2^+ \rightleftarrows O^+ + O_2$ (reaction 37) and $N_2 + N^+ \rightleftarrows N_2^+ + N$ (reaction 40) were used. Up to about $s/d_N = 0.5$ these two reactions were transferring charge from left to right, as evidenced by the fact that O^+ was growing and N^+ was decreasing. Transfer from right to left at larger values of s/d_N was ineffective in reducing O^+ because the concentration of O_2 was small compared to O^+. In similar fashion, the small amount of N_2^+ relative to N^+ made negligible any addition to N^+ by means of reaction 40.

It is evident from Fig. 7 that the electron concentration profiles on the aft part of the body can be in error if an inadequate charge transfer system is used. Figure 8, which shows profile shapes calculated for altitude = 156,000 ft, $x/d_N = 4$, illustrates this point.

D. Short vs Long Reaction Systems for Air

Since the types of charged particles present in air are different at high and low speeds, it is useful to consider choosing between short or long systems of chemical kinetic reactions. At low entry speeds (less than about 20,000 fps) the NO^+ ion is dominant in all parts of the flow. At high entry speeds (greater than about 30,000 fps) O^+ and N^+ ions are dominant. The transition between these extremes is not sharply defined. The reaction $N + O \rightleftarrows NO^+ + e^-$ is the fastest producer of ions in air up to about 30,000 fps,[14] but a large fraction of NO^+ ions transfer their charge to other species. In cool parts of the flowfield charge transfers back to NO^+, because the NO molecule has the lowest ionization potential of any of the species present.

If the NO^+ ion is the only one present in appreciable numbers, then computed results obtained with the 54 reaction (normal) system described earlier are indistinguishable from

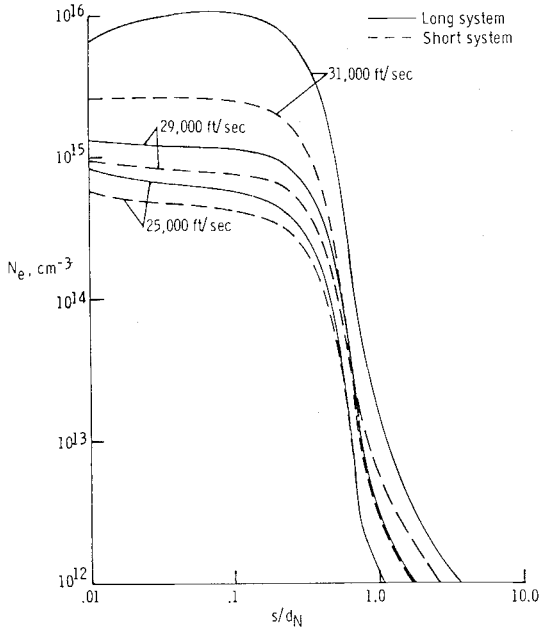

Fig. 9 Comparison of short and long reaction systems; body streamline, altitude = 156,000 ft.

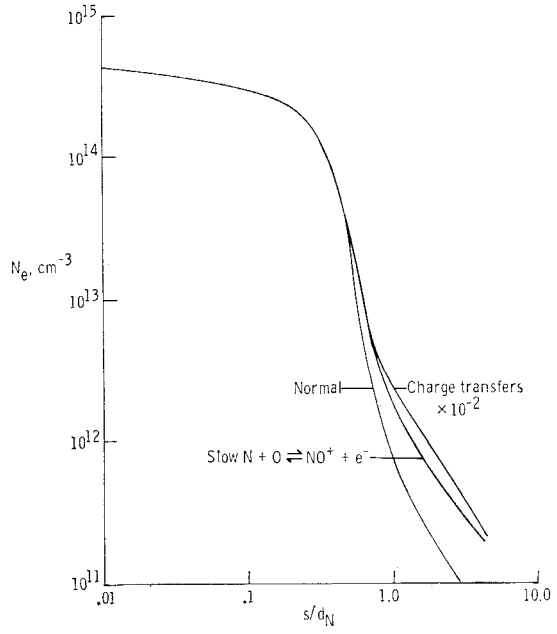

Fig. 10 Two examples of the effect of rate changes on streamline variation of electron concentration; body streamline, altitude = 175,000 ft.

those computed with a much simpler (short) system for which the species are O_2, N_2, O, N, NO, NO^+, e^- and the reactions are the 17 neutral reactions plus the reaction N + O $\rightleftarrows$ $NO^+ + e^-$. If O^+ and N^+ dominate, then the long (normal) system must be used. For intermediate speeds it is difficult to know beforehand that short and long system calculations will give the same results. However, the authors' experience has shown that profiles obtained from the two systems are often identical, particularly on the aft part of the body, where practically all species have transferred their charge to NO^+.

To illustrate this a typical variation of electron concentration along a streamline at an entry speed of 25,000 fps is shown in Fig. 9 for both short and long (normal) systems. Curves for the same streamline at entry speeds of 29,000 fps and 31,000 fps are also shown. At small values of s/d_N the results are not identical and the difference is larger at the higher speeds. This reflects the increased importance of atomic ions as speed increases. For all except 31,000 fps the curves for short and long (normal) systems merge at large values of s/d_N. Thus, except for 31,000 fps, profiles of electron concentration at body stations near the nose region would differ but profiles on the aft part of the body would not.

E. Sensitivity of Profiles to Reaction Rates

The curves shown in Figs. 10 and 11 are intended to illustrate that electron concentration profiles can be influenced by changing reaction rate constants. In Fig. 10 one curve was computed using the normal reaction system, in which the N + O $\rightleftarrows$ $NO^+ + e^-$ reaction (reaction 20) has been made three times faster[15] than the rate[16] most commonly used in recent years. Above the curve marked "Normal" lies one obtained with the slower rate for reaction 20. The fast rate causes the rise and fall of N_e to be more rapid. However, note that this can make a difference only if the charged particles are out of equilibrium with local concentrations and temperature. Thus, for small s/d_N the two curves are identical, but they split apart at large s/d_N. Local ionic equilibrium is present in the nose region, but on the aft part of the body the effect of the faster rate is visible.

The effect on the normal system of reducing all charge transfer rates (reactions 31–54) by a factor of 100 is shown in Fig. 10. The lag in recombining electrons here is caused by failure to transfer atomic ions as fast as the dissociative recombination reactions can dispose of them. Note the tendency for the gap between the curves to close at large s/d_N. This is because the reduction in charge transfer rates is not so critical in a region where dissociative recombination has begun to slow down.

The profiles of Fig. 11 show the effect of multiplying cross sections for the dissociation rates (reactions 1–15) by the factors 10 and 10^{-1}. The body station shown is $x/d_N = 4$, which is an aft station. It is interesting to note that changing the dissociation rate constants affects the slope of the profiles as well as the magnitude of the peak electron concentration. Also, it should be pointed out that, in contrast to the preceding examples in which ionic rates were changed, significant changes in calculated temperature are produced by changing the dissociation rates. These temperature

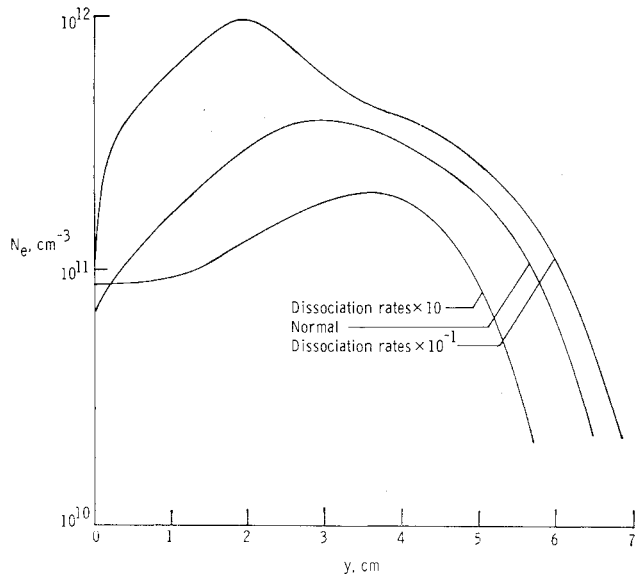

Fig. 11 Changes in the electron concentration profile caused by increasing and decreasing the dissociation rates; altitude = 175,000 ft, $x/d_N = 4$.

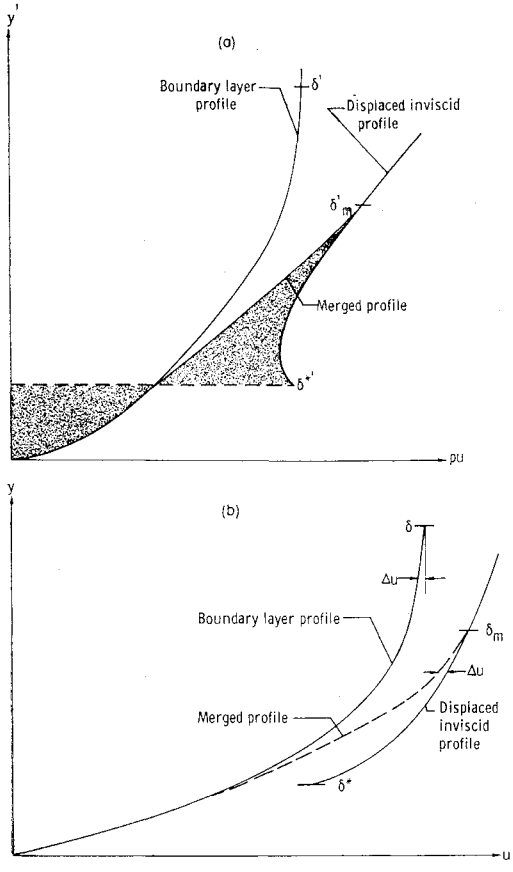

Fig. 12 Merging of inviscid and boundary-layer profiles.

changes, in turn, have a significant influence on the ionic chemistry.

Concluding Remarks

The uncoupled blunt-body nonequilibrium flowfield technique presented here is tailored to provide detailed ionization profiles in the supersonic portion of the flowfield. Use of the streamtube approach allows a comprehensive treatment of the ions and electrons, which are only trace species in the flow but which are all-important for radio attenuation problems. It is shown that the ion concentration can be sensitive to the chemical kinetics rates and to the completeness of the reaction system. Innovations in the technique have the effect of coupling the chemical kinetics to the flowfield solution so that the resulting profiles display effects due to boundary-layer displacement, streamline swallowing, and vorticity interaction. The technique is useful for computation of a large number of trajectory points for a given entry body, although computing time comparisons with other methods have not been made.

Appendix A: Mass Conservation Computer Program

The sketch in Fig. 1 should be helpful in understanding the derivation of the mass conservation equations. The basic idea is to equate the mass which flows through a specified area of the shock wave per unit time to a corresponding mass flow further downstream. The mass flow inside the body of revolution generated by rotating about the body axis the streamline whose entry point into the shock front is distant $(r_s)_i$ from the body axis is $\rho_1 u_1 (r_s)_i^2$.

The mass flow between the same body of revolution and the surface of the body at any downstream station (except those close enough to the nose that the streamlines are not even approximately parallel to the body surface) is

$$2\pi \int_0^{y_i} \rho u (r_b + y \cos\theta) dy$$

If these two mass flows are set equal to each other the unknown is y_i, the thickness of the gas layer. In this form the functions $\rho u = \rho u(y)$ and $y\rho u = y\rho u(y)$ must be integrated from the body surface to the streamline in question. The pitfalls inherent in automated curve fitting to obtain the required functions of y were avoided by formulating the problem in terms of increments of y between streamlines. For this the entering mass flow is $\rho_1 u_1 \pi [(r_s)_i^2 - (r_s)^2_{i-1}]$ and the corresponding mass flow downstream is

$$2\pi \int_0^{dy_i} \rho u [r_b + (y_{i-1} + y) \cos\theta] dy$$

Let $A_i^2 = (r_s)_i^2 - (r_s)^2_{(i-1)}$, and $B_i = r_b/\cos\theta + y_{i-1}$ Then,

$$\rho_1 u_1 A_i^2 = 2 \cos\theta \int_0^{dy_i} \rho u [B_i + y] dy$$

Let $\hat{y} = y/dy_i$, $\hat{\rho}\hat{u} = \rho u/\rho_1 u_1$,

$$\psi_i = \left(\int_0^1 \hat{\rho}\hat{u} d\hat{y}\right)_i, \quad \phi_i = \left(\int_0^1 \hat{\rho}\hat{u}\hat{y} d\hat{y}\right)_i$$

Then,

$$\frac{dy_i}{2B_i} = -\frac{\psi_i}{\phi_i} + \left[\frac{\psi_i^2}{\phi_i^2} + \frac{2}{\phi_i \cos\theta} \frac{A_i^2}{B_i^2}\right]^{1/2} \tag{A1}$$

This equation expresses the value of the increment in y, dy_i, between streamlines i and $i-1$ in terms of the y coordinate for the preceding streamline, y_{i-1}, and the integrals ψ_i and ϕ_i. The values of ρ and u are already known at $\hat{y} = 0$ and at $\hat{y} = 1$, because these are network points. By assuming that $\hat{\rho}\hat{u}$ varies linearly with $\hat{y}$ in the range $0 < \hat{y} < 1$, the integrals can be evaluated as follows:

$$\left(\int_0^1 \hat{\rho}\hat{u} d\hat{y}\right)_i = \frac{1}{2}[(\hat{\rho}\hat{u})_{i-1} + (\hat{\rho}\hat{u})_i] \tag{A2}$$

$$\left(\int_0^1 \hat{\rho}\hat{u}\hat{y} d\hat{y}\right)_i = \frac{1}{2}[(\hat{\rho}\hat{u})_{i-1}] + \frac{1}{3}[(\hat{\rho}\hat{u})_i - (\hat{\rho}\hat{u})_{i-1}] \tag{A3}$$

Appendix B: Details of Boundary-Layer Treatment

Boundary-Layer Profiles and Displacement Effects

Initial boundary-layer profiles are calculated from laminar similar solutions for an axisymmetric body at zero yaw.[17] The results from these solutions are used in two ways: 1) at each body station the boundary-layer displacement thickness δ^* is added to the y coordinate of each streamline outside the boundary layer, and 2) the profiles of ρu and u are merged with corresponding profiles in the displaced inviscid flowfield. Nonequilibrium edge conditions are used, and the program assumes that boundary-layer gas properties are thermally frozen (i.e., no dissociation or recombination of atoms occurs in the boundary layer). This assumption is reasonably good for finding thermal properties (not ionization), as chemical kinetics computations show very little change in atom concentration occurs in the bulk of the boundary layer aft of the shoulder in the altitude regime where boundary-layer effects are significant. Even near the wall where atom recombination will actually occur the error is quite small, since T and ρ in this region must approach the cold-wall values as specified by the ablation temperature. Use of local nonequilibrium edge properties for the boundary layer gives better results than use of either equilibrium or frozen-flow edge properties (as in a complete blunt-body program), since, in general, processes behind the

shock and in the expansion around the body are far from either.

Initial nonequilibrium edge properties are taken from the inviscid, body streamline calculations. Then, since the boundary layer is thick, swallowing of the inviscid streamlines into the boundary layer is taken into account in choosing edge conditions along the boundary layer for a repeat calculation. The criterion for swallowing a given streamline is based on equality of the boundary-layer mass flow to the entering mass flow. For stations in the nose region, let $y' = y(1 + y/d_N)$. Then

$$\rho_1 u_1 \pi (r_s)_i^2 = \pi d_N \cos\theta_b \int_0^{y'} \rho u dy' \tag{B1}$$

In the region aft of the shoulder, let $y' = y[1 + (\cos\theta_c/2)(y/r_b)]$. Then

$$\rho_1 u_1 \pi (r_s)_i^2 = 2\pi r_b \int_0^{y'} \rho u dy' \tag{B2}$$

The first use of the boundary-layer solutions is to provide values of δ^* which are added to the body dimensions and thus displace the inviscid shock layer. A plot of the new shock shape is used to provide new starting angles and pressure for the entering streamlines. Also, an effective cone angle and nose diameter are determined which, along with use of the normalized flowfield inputs previously discussed, allows new pressure distributions along the streamlines to be found. The new pressure distributions are used to recompute the inviscid nonequilibrium shock layer properties and streamline locations, and the whole cycle can be repeated until satisfactory agreement is obtained between input and output shock shape and streamline position.

Merged Profiles

Flow vorticity was accounted for partially in the preceding step, where edge properties were chosen by means of a swallowing criterion. An additional correction for the vorticity normal to the flow direction is obtained by merging boundary-layer profiles with displaced inviscid flow profiles.

Merging is carried out for the ρu and u shock layer profiles, and three principal criteria are applied in the merging procedure: 1) mass conservation for the ρu profiles, 2) velocity defect for the u profiles, and 3) smooth transition for both from the displaced inviscid profile (in the neighborhood of $y = \delta$) to the boundary-layer profile (in the neighborhood of $y = \delta^*$). In Fig. 12a where a typical ρu profile has been plotted against the transformed coordinate y', equality of the shaded areas indicates that the mass flow is the same whether obtained by integrating the merged or the displaced inviscid profile. In addition to respecting the mass-flow criterion, the merged profile is required to blend smoothly into the two original profiles.

Figure 12b illustrates the merging of the velocity profiles. The velocity defect inside δ_m (δ_m was determined in step 1) on the merged profile is made similar to that within the boundary-layer profile. This velocity defect criterion is applied only for the outer region of the profile, since the inner profile must merge into the boundary-layer profile.

Boundary-Layer Streamtubes and Matching Conditions

The next step in the flowfield determination is to identify "streamline" positions inside the merged boundary layer so that the matching parameters for use in the boundary-layer nonequilibrium streamtube analysis may be evaluated. This is done by integrating the ρu vs y' merged profiles to find those values of y' within which mass flow equals that of each entering streamline. With streamline positions established in the boundary layer, values of the matching conditions are read from merged plots of ρu and u at each body station. These values, along with the pressure matching parameters (which are assumed to be unchanged from those of the corresponding displaced inviscid streamlines)-are used in the boundary-layer version of the streamtube program. Profiles of species concentration can then be con, structed at each body station. It should be pointed out that the specification of p and ρ in the boundary-layer streamtube analysis is nearly equivalent to specifying the temperature T, within the altitude range where the boundary layer is significant. In this range the composition changes in the boundary layer involve principally electrons and ions, with no significant alteration of the neutral species concentration. Because the chemical kinetics depends strongly on temperature, it is important that the boundary layer and matching conditions be determined using finite rate considerations so that the temperature in the boundary layer is correctly specified.

The profiles of electron and ion concentrations which are obtained by the methods described here do not contain effects of surface recombination or of diffusion of ionic species, and therefore restrict the validity of calculations for the body considered herein to altitudes below about 230,000 ft.

References

[1] Blottner, F. G., "Nonequilibrium Laminar Boundary-Layer Flow of Ionized Air," *AIAA Journal*, Vol. 2, No. 11, Nov. 1964, pp. 1921–1927.

[2] Pallone, A. J., Moore, J. A., and Erdos, J. I., "Nonequilibrium Nonsimilar Solutions of the Laminar Boundary-Layer Equations," *AIAA Journal*, Vol. 2, No. 10, Oct. 1964, pp. 1706–1713.

[3] Kaplan, B., "The Nonequilibrium Air Boundary Layer on a Blunt Nosed Body," TIS-68SD227, April 1968, General Electric Space Sciences Lab., King of Prussia, Pa.

[4] Dellinger, T. C., "Computation of Nonequilibrium Merged Stagnation Shock Layers by Successive Accelerated Replacement," AIAA Paper 69-655, San Francisco, Calif., 1969.

[5] DeRienzo, P. et al., "Effects of Nonequilibrium on the Hypersonic Laminar Boundary Layer," Research Rept. 171, Sept. 1963, Avco-Everett Research Lab., Everett, Mass.

[6] Webb, H., Jr. et al., "Theoretical Flow Field Calculations for Project RAM," CR-1308, May 1969, NASA.

[7] Holt, M., "Direct Calculation of Pressure Distribution on Blunt Hypersonic Nose Shapes with Sharp Corners," *Journal of the Aerospace Sciences*, Vol. 28, No. 11, Nov. 1961, pp. 872–876.

[8] Lomax, H. and Inouye, M., "Numerical Analysis of Flow Properties about Blunt Bodies Moving at Supersonic Speeds in an Equilibrium Gas," TR R-204, July 1964, NASA.

[9] Hall, J. G., Eschenroeder, A. Q., and Marrone, P. V., "Blunt-Nose Inviscid Airflows with Coupled Nonequilibrium Processes," *Journal of the Aerospace Sciences*, Vol. 29, No. 9, Sept. 1962, pp. 1038–1051.

[10] Blick, E. F. and Francis, J. E., "Spherically Blunted Cone Pressure Distributions," *AIAA Journal*, Vol. 4, No. 3, March 1966, pp. 547–548.

[11] Lomax, H. and Bailey, H. E., "A Critical Analysis of Various Numerical Integration Methods for Computing the Flow of a Gas in Chemical Nonequilibrium," TN D-4109, Aug. 1967, NASA.

[12] Hansen, C. F., "Estimates for Collision-Induced Dissociation Rates," *AIAA Journal*, Vol. 3, No. 1, Jan. 1965, pp. 61–66.

[13] Lin, S. C. and Teare, J. D., "A Streamtube Approximation for Calculation of Reaction Rates in the Inviscid Flow Field of Hypersonic Objects," Research Note 223, Aug. 1961, Avco-Everett Research Lab., Everett, Mass.

[14] Wilson, J., "Ionization Rate of Air Behind High-Speed Shock Waves," *The Physics of Fluids*, Vol. 9, No. 10, Oct. 1966, pp. 1913–1921.

[15] Dunn, M. G. and Lordi, J. A., "Measurement of $NO^+ + e^-$ Dissociative Recombination in Expanding Air Flows," Rept. Al-2187-A-10, Sept. 1968, Cornell Aeronautical Lab., Buffalo, N.Y.

[16] Lin, S. C. and Teare, J. D., "Rate of Ionization Behind Shock Waves in Air. II. Theoretical Interpretations," *The Physics of Fluids*, Vol. 6, No. 3, March 1963, pp. 355–375.

[17] Cohen, N. B., "Boundary-Layer Similar Solutions and Correlation Equations for Laminar Heat-Transfer Distribution in Equilibrium Air at Velocities up to 41,000 Feet Per Second," TR R-118, May 1961, NASA.